Supporting Information

Wood-Inspired Bimodal Solar-Driven Evaporator for Highly Efficient and Durable Purification of High-Salinity Wastewater

Yu Chen[a,b], Jin Yang[a]*, Dongfang Zhang[a], Sizhe Wang[a], Xiaohua Jia[a], Yong Li[a], Dan Shao[a], Lei Feng[a], Haojie Song[a]*, Shaochun Tang[b]*

[a]*School of Materials Science & Engineering, Shaanxi Key Laboratory of Green Preparation and Functionalization for Inorganic Materials, Shaanxi University of Science & Technology, Xi' an, Shaanxi, 710021, P.R. China*

[b]*National Laboratory of Solid State Microstructures, Collaborative Innovation Center of Advanced Microstructures, Jiangsu Key Laboratory of Artificial Functional Materials, College of Engineering and Applied Sciences, Nanjing University, Nanjing 210093, P. R. China.*

*E-mails: yangjin@sust.edu.cn; songhaojie@sust.edu.cn; tangsc@nju.edu.cn

Contents

Experimental section.

1. Chemicals and materials

Balsa wood and artificial seawater were obtained from Alibaba (China). Hydrochloric acid (HCl) and acetic acid were purchased from Macklin Biochemical Co., Ltd. (China). Sodium chlorite ($NaClO_2$, 80%) was obtained from Aladdin Biochemical Technology Co., Ltd (China). $Ti_3C_2T_x$ MXene was supplied by 11 Technology Co., Ltd., (China). Glutaraldehyde (25.0-28.0%) was produced by Shanghai Meryer Chemical Reagent Co., Ltd., (China). PVA with an average molecular weight of 13000-23000 was purchased from Sigma-Aldrich.

2. Preparation of WBE

2.1 Preparation of CNFs from natural wood

Natural wood blocks were initially delignified lignin via immersing in an acetic acid buffered containing 2 wt% $NaClO_2$ at 100 °C for 6 h. Then, the treated samples were extracted with 4 wt% NaOH solution at 80 °C for 4 h to form cellulose suspension. The obtained cellulose suspension was suction filtered and washed with deionized water 2 to 3 times to remove internal chemical reagents. The suspension was freeze-dried to obtain a cellulose block (-80 °C, 40 h), and then crush with a mechanical crusher to obtain CNFs.

2.2 Fabrication of cross-linked CNFs/PVA and CNFs/PVA/MXene suspension

First, 20 mL of PVA solution (3.5 wt%) and 0.3 g of CNFs were continuously stirred at 90 °C for 30 min until fully dissolved to obtain a CNFs/PVA precursor suspension. Then, 1 ml HCl solution (1.2 M) and 200 μl Glutaraldehyde were added to the precursor

solution and stir evenly to obtain a cross-linked CNFs/PVA suspension. The procedure of preparing cross-linked CNFs/PVA/MXene suspension is consistent with that of the CNFs/PVA suspension, except for adding 5 wt% of MXene in CNFs.

2.3 Preparation of WBE

WBE was fabricated via the ice-template induced self-assembly method. First, 15 mL of the cross-linked suspension was poured into a custom-made glass cup (diameter ≈3 cm) and freeze it at -80 °C for 40 min. Afterward, 5 mL of cross-linked CNFs/PVA/MXene suspension was adcccded in the frozen CNFs/PVA glass cup. Note that, before adding the cross-linked CNFs/PVA/MXene suspension, slightly dissolve the ice on the surface of the frozen CNFs/PVA to promote the combination of the two phases. The glass cup was frozen at 80 ℃ for 1 h, and then thaw it in deionized water at room temperature to obtain WBE. Actually, since the density of CNFs is much lower than that of PVA, the relative content of CNFs/PVA in the constructed system of WBE is 3:7. WBE-1 and WBE-2 only need to change the relative content of cross-linked CNFs/PVA to 1:9 and 1:1.

3. Materials characterization

The microstructure of the samples was observed on a scanning electron microscopy (SEM, Hitachi SU−8100, Japan). Nicolet iS10 FTIR spectrometer (USA) was applied to obtain attenuated total reflection Fourier transformed infrared spectroscopy (ATR−FTIR) spectra. X-ray diffraction patterns (XRD) of samples were measured on a Bruker D8 Advance (Japan) at 40 kV (100 mA). The thermal conductivity of all samples was conducted by laser thermal conductivity meter (NETZSCH LFA 457, Germany).

Absorption spectra and transmittance of all samples were measured using a UV-Vis-NIR spectrometer (Cary 5000, Germany). Raman spectra were measured via spectrometer (WITec alpha300). The concentration of Na^+, K^+, Ca^{2+}, Mg^{2+} of evaporated seawater was confirmed by inductively coupled plasma mass spectrometry (ICP-MS, Agilent 7500ce, USA). The vaporization behavior of WBE were observed by a TAQ2000 DSC (heating rate: 5 °C min^{-1}).

4. Solar evaporation measurement

The indoor steam generation process was monitored in a glass bottle with a diameter of 4.0 cm and a height of 8 cm (ambient temperature ≈ 25 ℃, humidity ≈ 50%). The height of the test liquid in the glass bottle is 6 cm. The experiments were conducted using CEL-S500 solar simulator as the light source. WBE samples were fixed in the center of the glass vial by polystyrene foam for testing. The mass change of evaporated water was measured by an electronic balance (accuracy: 0.0001 g), and the data were recorded by computer for further analysis of evaporation performance. All evaporation performance results were measured after a stabilization under 1 sun for 1 h.

Section S1. Numerical simulation

COMSOL Multiphysics 5.4 software package was used to simulate the heat transfer, salinity distribution, and brine transport in a wood-inspired bimodal evaporator (WBE) during solar desalination.

1. 1 COMSOL simulation of thermal conduction and temperature distribution in WBE.

Along with the previous report, the heat transfer model can be simplified as a semi-

infinite medium for the Cartesian coordinate system. Considering the presence of water molecules in the capillary channel, the heat transfer in the 3D porous structure can be calculated by the equation given below describe: [1]

$$E_{in} = \rho C_p \frac{\partial T(x,t)}{\partial t} + \rho C_p v \cdot \nabla T(x,t) + \nabla[k \nabla T(x,t)] \quad (1)$$

Where the E_{in} represents the thermal energy input from the optical-thermal conversion; T(x, t) is the local temperature; x and t are the space vector and time, respectively, and are the volume fraction, mass density and thermal capacity of doped polymer, ν, ρ, and C_p are the fluid flow speed, liquid mass density, and its thermal capacity, respectively. The numerical simulations are conducted by COMSOL Multiphysics under the steady and transient analysis mode. The overall thermal conductivity of WBE used here is the experimental result as shown in Figure 4b. To carry out a qualitative analysis, we assume that the temperature of the environment and water was set to 25 ºC (293 K). The relevant parameters of water directly came from the material library of COMSOL Multiphysics.

1. 2 COMSOL simulation of salinity distribution in the WBE.

To simulate the diffusion and convection of the salt ions in the internal microstructure of 3D evaporator, and then observe the distribution of the salt concentration in each part of the WBE, we simulated the internal mass transfer process of WBE. The simulation could be obtained by the following formulae:[2]

$$\nabla J_j + u \cdot \nabla c_j = R_j \quad (2)$$

$$J_j = - D_j \nabla c_j \quad (3)$$

Where $\boldsymbol{J}_j$ is the mass flux relative to the mass averaged velocity, **u** is the mass averaged velocity vector, c_j is the concentration of the species, R_j is a reaction rate

expression for the species, D_j is the diffusion coefficient. The salt concentration of the underlying bulk brine was set to 20 wt%.

1. 3 COMSOL simulation of brine transport in the WBE.

The numerical simulation of the velocity field of brine flow in porous media takes into account the longitudinal solute capillary action between the evaporative interface and water, gravity, thermal capillary action, and lateral solute capillary action at the evaporative interface, where the brine inlet is set at the bottom of the evaporator. The numerical simulation system was analyzed by processing a Multiphysics situation coupled with the Laminar Flow Module and Fluid Heat Transfer Module. The water transport process could be illustrated by solving the following equations:

Laminar flow analysis:

$$\rho\frac{\partial_u}{\partial_t} + \rho(u \cdot \nabla)u = \nabla \cdot [-pI + K] + \rho g \tag{4}$$

$$\frac{\partial_\rho}{\partial_t} + \rho\nabla \cdot (u) = 0 \tag{5}$$

$$K = \mu \cdot (\nabla u + (\nabla u)^T) \tag{6}$$

Fluid heat transfer analysis:

$$Q = d_z\rho C_p\frac{\partial T}{\partial t} + d_z\rho C_p u \cdot \nabla T + \nabla \cdot q \tag{7}$$

$$q = -d_z k\nabla T \tag{8}$$

where **u** represents the velocity field (m s^{-1}), both in laminar flow and heat transfer, ρ is the water density (kg m^{-3}), p is the pressure (Pa), **I** is the constitutive relation coefficient, and **K** is the water viscosity. μ is denoted as the dynamic viscosity, ϱ w is an automatic wall distance parameter; C_p is the water capacity at constant pressure (J kg^{-1} K^{-}

[1]); **q** is the conductive heat flux (W m^{-2}) and g is the gravity (N).

Section S2. Dark evaporation experiment to estimate the vaporization enthalpy of WBE.

Inspired by the reduced water vaporization enthalpy of hydrogel materials reported by Yu et al., [3,4] we conducted control experiments to estimate the vaporization enthalpy of water in WBE. Specifically, two beakers with a diameter of 3 cm are used as containers, where one container is filled with water, and the other container is filled with WBE containing saturated water. The two containers are placed in a constant temperature airtight box simultaneously to avoid the influence of air convection on the evaporation rate. It is worth noting that the entire experiment (more than 10 h) was carried out in a dark environment, and the mass loss of each glassware was recorded to estimate the solar evaporation rate. The above experiment was repeated 6 times to calculate the evaporation rate, as shown in the table below.

Table S1

Test	Room Temperature (℃)	Water Temperature (℃)	Evaporation rate of water (g m^{-2} h^{-1})	Evaporation rate of WBE (g m^{-2} h^{-1})	Evaporation rate ratio (water/ WBE)
1	24-26	20-22	82.6	164.5	0.5022
2	24-26	20-22	79.5	162.5	0.4892
3	24-26	20-22	74.8	158.7	0.4712
4	21-23	18-20	67.9	136.3	0.4982
5	21-23	18-20	63.2	130.4	0.4847
6	21-23	18-20	66.0	127.6	0.5173

To calculate the equivalent vaporization enthalpy of water in WBE, we hypothesized that under the same ambient temperature and pressure, the evaporation rate and vaporization enthalpy of pure water and WBE satisfy the following equation:

$$E_{WBE}M_{WBE}=E_{water}M_{water} \quad (9)$$

where E_{WBE} and M_{WBE} are the vaporization enthalpy and evaporation rate in WBE, E_{water} and M_{water} are the vaporization enthalpy and of pure water, respectively. Calculated based on the average of 6 tests, M_{water}/M_{WBE} is about 0.4938. Using the reported vaporization enthalpy of pure water (~2436.4 J/g), the equivalent vaporization enthalpy of water in WBE can be calculated to be 1203.8 J/g based on the data in the above table. Similarly, the estimated vaporization enthalpies of WBE-1 and WBE-2 in the dark evaporation experiment are shown in the following:

Table S2. Comparison of vaporization enthalpy from DSC measurement and dark experiment.

Enthalpy (J/g)	Pure water	WBE-1	WBE	WBE-2
DSC measurement	2440	1656	1325	1198
Dark experiment	2436.4	1387.3	1203.8	1018.4

The DSC measured enthalpy of water is 2440 J/g, which is very close to the theoretical value of 2436.4 J/g, indicating the accuracy of our measurements. This enthalpy value for water in WBE is considerably higher than that estimated from the dark experiment discussed previously, due to the in DSC measurement being a complete dehydration process, whereby the water-polymer configuration changes significantly between a swelled state and a dehydrated state. For the dark experiment, weakly bonded

water molecules in cellulose are constantly replenished through diffusion from the water reservoir, a process that more closely resembles that of the actual solar evaporation application.

Section S3. The solar evaporation efficiency caculations.

The conventional method of solar evaporation was used to further evaluate the solar evaporation efficiency (η) of WBE, which was described by the following formula:

$$\eta = \nu \cdot (H_e + Q) / C_{opt} \cdot P_0 \quad (10)$$

where ν is the evaporation rate while reaching steady-state condition (dark evaporation rate of 0.27 kg m^{-2} h^{-1} was subtracted), H_e is the enthalpy change in the process of water molecules vaporization, and Q is the sensible heat per unit mass of water. C_{opt} is the optical concentration of photothermal interface, and P_0 is the 1 sun illumination power (1 kW m^{-2}). The obtained calculation results indicated that the evaporation efficiency of WBE was approx. 91.8%.

Meanwhile, the energy efficiency of WBE is further confirmed according to the law of thermodynamic energy conservation. Under solar irradiation, the energy loss of the solar evaporation system mainly includes three ways: 1) radiation loss (P_{rad}), 2) convection loss (P_{conv}), and 3) conduction loss (P_{cond}). Detailed energy loss analysis was performed as following calculations.

(1) Radiation loss:

The radiation flux P_{rad} can be calculated by Stefan-Boltzmann law.

$$P_{rad} = \varepsilon A \sigma (T_1 - T_2) \quad (11)$$

Where P rad denotes radiation heat flux, ε is the emissive rate (It is assumed that the absorber has a maximum emissivity of 1.00), A is the surface area, σ is the Stefan-Boltzmann constant (assumed to be 5.67×10^{-8} W m^{-2} K^{-4}), T_1 is the average temperature of the absorber (~35.7 °C), and T_2 is the ambient temperature (~31.6 °C). As a result, the radiation heat flux is estimated to be 26 W m^{-2}, and the radiation loss rate is about 2.6%.

(2) Convection loss:

The convection loss P conv can be calculated by Newton's law of cooling.

$$P_{conv} = h_1 (T_1 - T_2) + h_2 (T_2 - T_3) \quad (12)$$

Where P conv denotes convection heat flux, h_1 and h_2 are the convection heat transfer coefficient (PVA/CNFs/MXene assumed to be 0.62 W m^{-2} K^{-1}, and PVA/CNFs assumed to be 0.24 W m^{-2} K^{-1}, respectively), T_1 and T_2 are 35.7 and 32.9 ℃ T_3 is the temperature of the bulk water (~25 °C). Here, the convection heat is estimated as ≈ 4 W m^{-2} , and the convection loss rate is about 0.4%.

(3) Conduction loss:

Conduction loss P_{cond} is based on Fourier's law.

$$P_{cond} = C \cdot m \Delta T \quad (13)$$

Where C is the specific heat capacity of water (4.2 J K^{-1} g^{-1}), m denotes the weight of bulk water and ΔT represents the increased temperature of the bulk water after stable steam generation. In this work, m = 60 g, ΔT = 1.5 ℃. Thus, the conductive loss is about 52 W m^{-2} and the conductive heat loss rate is about 5.2 %.

Therefore, the evaporation efficiency of WBE was calculated as 91.8% (1-2.6%-0.4%-5.2%=91.8%). This is consistent with the results of evaporation efficiency

calculated by evaporation rate, confirming the effectiveness of energy conversion during the evaporation process.

Table S3. Comparison of solar steam generation performance and energy efficiency between our WBE and other previously reported evaporators.

Sample	Temperature (℃)	Evaporation rate (kg m^{-2} h^{-1})	Efficiency (%)	Reference
Poly(vinyl alcohol) film	40.5	1.50	91.5	5
Porous polymer	47.4	1.67	90.3	6
MoS_2/SA@MF sponge	45.9	1.81	90.0	7
Cellulose monolithic	38.0	1.82	89.9	8
Macroporous membrane	45.0	2.045	93.1	9
PVA hydrogel	37.0	2.08	85.6	10
Carbon hybrid aerogel	45.6	2.12	89.8	11
PVA/SA/PAAM hydrogel	42.5	2.21	91.4	12
Janus aerogels	53.5	2.287	88.2	13
CS/PAAm/PPy hydrogel	39.5	2.41	92.0	14
T-shaped wood	53.7	2.43	83.6	15
WBE	35.7	3.02	91.8	This work

Table S4. Salt resistance performance of WBE compared with other materials.

Reference	Salinity (%)	Time (h)	Evaporation rate (kg m^{-2} h^{-1})	Efficiency (%)
17	10	10	1.50	80.0
18	10	48	1.57	88.9
29	10	200	1.59	89.6
20	15	6	1.3	80.0
21	20	100	1.04	75.1
2	20	1	1.25	\
22	20	8	2.07	\
13	21	5	1.97	\
9	25	2	1.69	\
WBE	20	100	2.48	81.0

1. Preparation and characterization of CNFs.

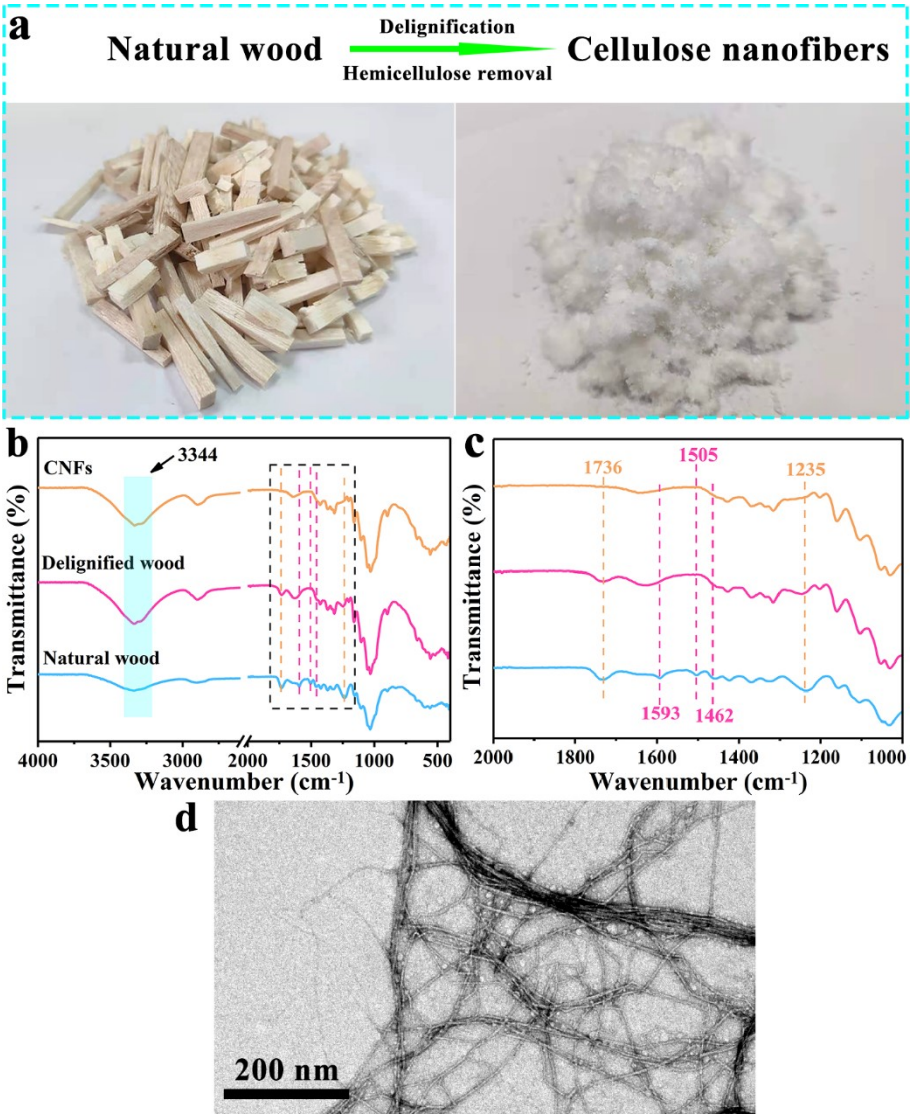

Figure S1. (a) Optical photos of natural wood and CNFs. (b, c) ATR-FTIR spectra of natural wood, delignified wood and CNFs. The characteristic peaks of lignin at 1593, 1505, and 1462 cm^{-1}, and the peaks of hemicellulose at 1736 and 1235 cm^{-1} disappeared after the chemical treatment. (d) TEM images of prepared CNFs, with a diameter about 20 nm.

2. Preparation process of layered CNFs suspension.

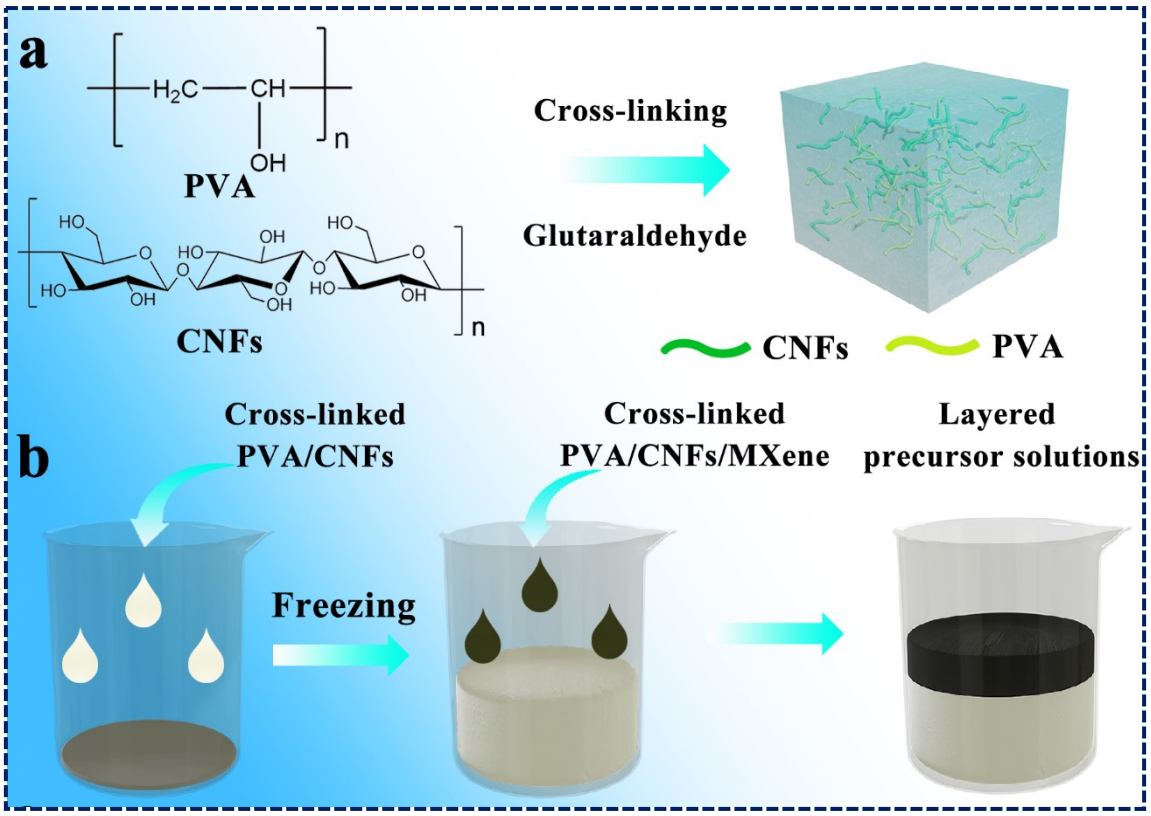

Figure S2. The preparation process of layered CNFs suspension. First, CNFs and PVA were first cross-linked with GA under acidic conditions, where the aldehyde group of GA undergoes aldol condensation reaction with the abundant hydroxyl functional groups of CNFs and PVA, forming CNFs/PVA precursor suspension with hydrogen bonding and chemical cross-linking (Figure S3a). Then, 15 mL of the cross-linked suspension was poured into a custom-made glass cup (diameter ≈3 cm) and freeze it at -20 °C for 30 min, until the suspension surface is slightly frozen. Afterward, 5 mL of cross-linked CNFs/PVA /MXene suspension was added in the frozen CNFs/PVA glass cup to form a layered CNFs suspension (Figure S3b). Note that, before adding the cross-linked CNFs/PVA/MXene suspension, slightly dissolve the ice on the surface of the frozen CNFs/PVA to promote the combination of the two phases.

3. ATR-FTIR characterization of different samples.

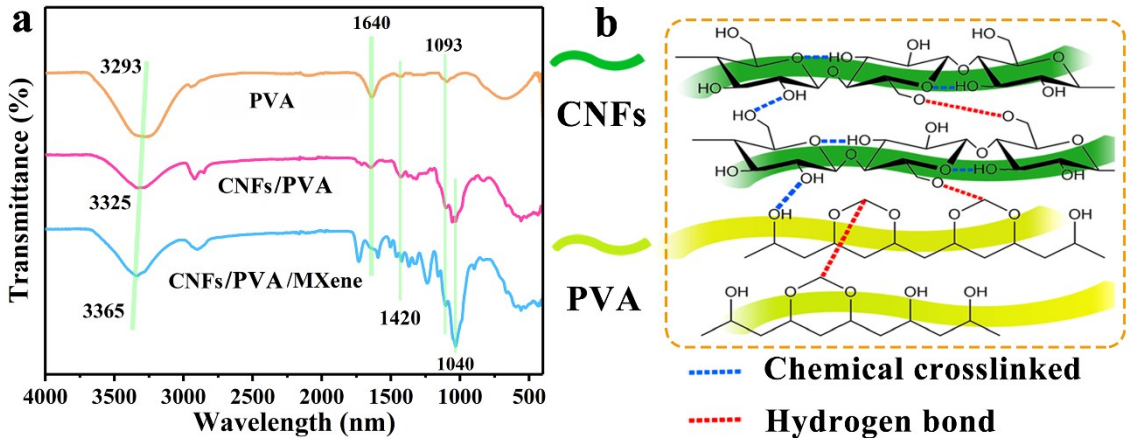

Figure S3. (a) ATR-FTIR spectra of pure PVA, CNFs/PVA, and CNFs/PVA/MXene. (b) Schematic diagram of binding and bonding of CNFs, PVA, and GA.

ATR-FTIR spectra were applied to confirm the successful combination of CNFs/PVA/MXene. For PVA, the peak at 1093 cm^{-1} could be attributed to the C-O tensile vibration formed after PVA and GA were cross-linked. Since the compounding of CNFs, CNFs/PVA and CNFs/PVA/MXene exhibited a new peak at 1040 cm^{-1} corresponding to the C-O-C stretching vibration of the β-glycosidic bond between the glucose rings. Two peaks near 2900 and 1420 cm^{-1} were attributed to the stretching and bending modes of the C-H bond. Moreover, two common peaks at 1640 and 3330 cm^{-1} showed a common band corresponding to the stretching, bending and deformation vibrations of the hydroxyl group, in which the deviation of the peak position at 3330 cm^{-1} is most possibly due to the formed hydrogen bond with combination of CNFs and MXenes.

4. XRD characterization of different samples.

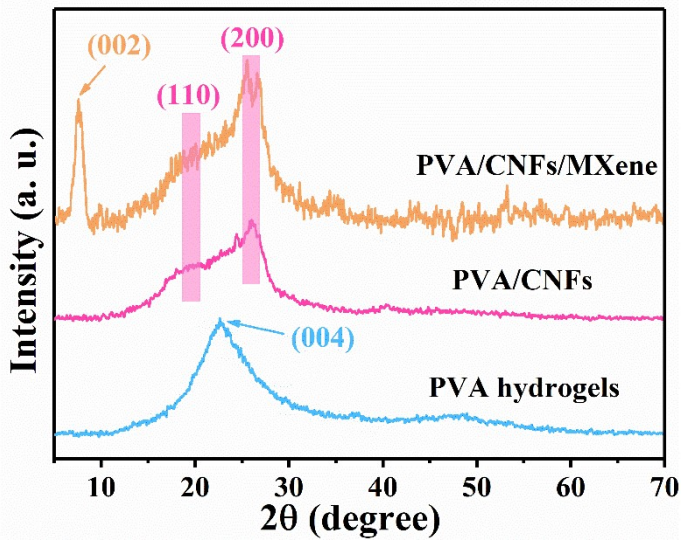

Figure S4. XRD spectra of PVA hydrogels, PVA/CNFs, and PVA/CNFs/MXene sample. For pure PVA hydrogel, a broad peak was observed at 22.42° was assigned to the (400) crystal plane of the PVA network. With the addition of CNFs, two peaks appeared at 20.62 and 26.18°, which were attributed to the (110) and (200) crystal planes of cellulose, respectively. After compounding with MXenes, the crystal plane of cellulose can still be clearly observed, and a new sharp peak was found at 7.96°, which is assigned to the (002) crystal plane of MXenes.

5. Optical photos of WBE.

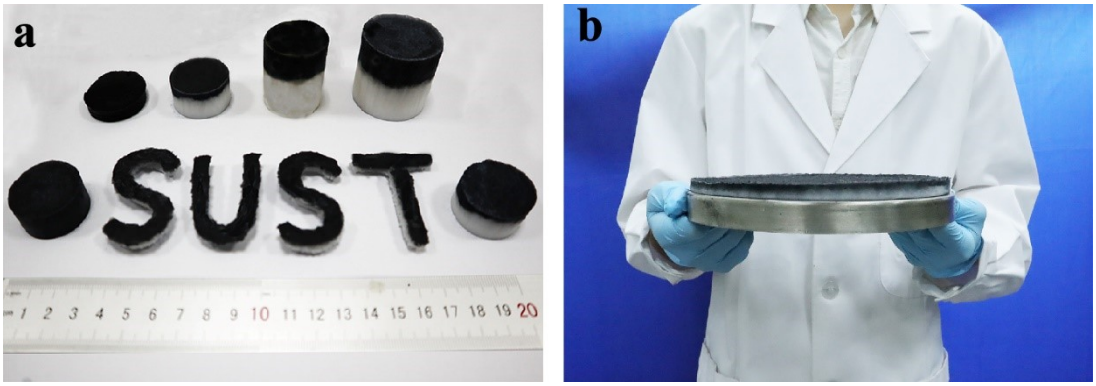

Figure S5. Optical photos of (a) various complex shapes, and (b) side-view of large-scale WBE with a volume of approx. 1.0×10^3 cm^3.

6. SEM characterization of natural balsa wood.

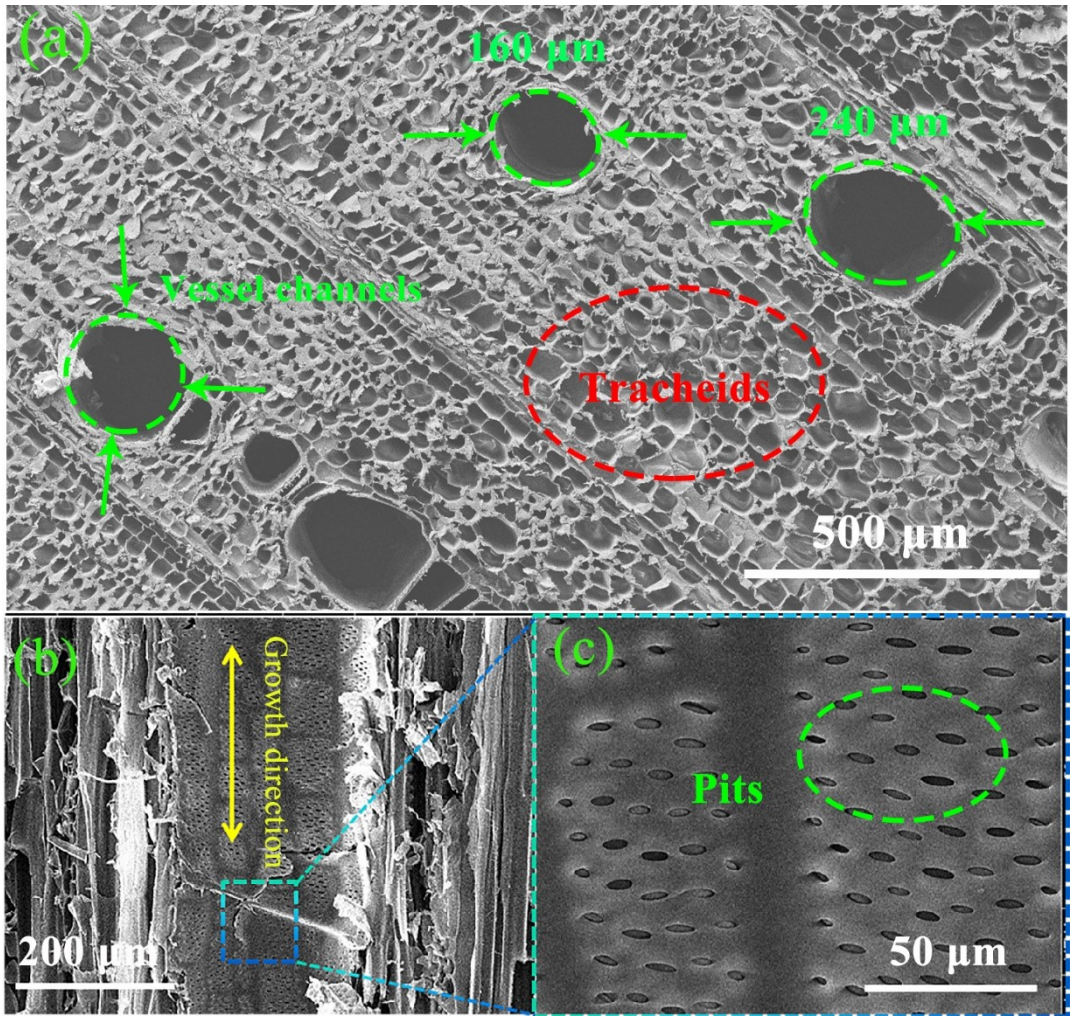

Figure S6. (a) Top view SEM image of balsa wood shows numerous wide vessel channels and comparatively narrow tracheids along the tree growth direction. (b) Side view SEM image of balsa wood shows ray cells periodically penetrate the microchannels. (c) Magnified side view SEM image of one wide vessel channel, numerous pits are present on the cell walls, which can also help lateral brine transport.

7. The water transfer capability of WBE.

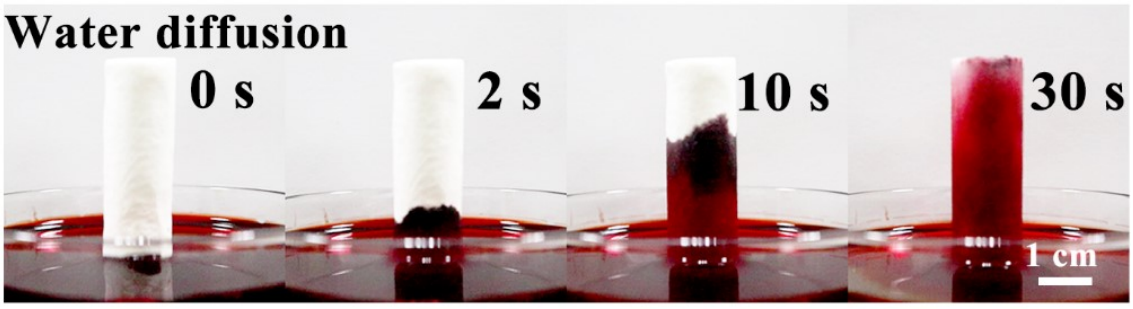

Figure S7. Dye solution absorption capacity of water diffusion layer.

8. COMSOL transient simulation of WBE model.

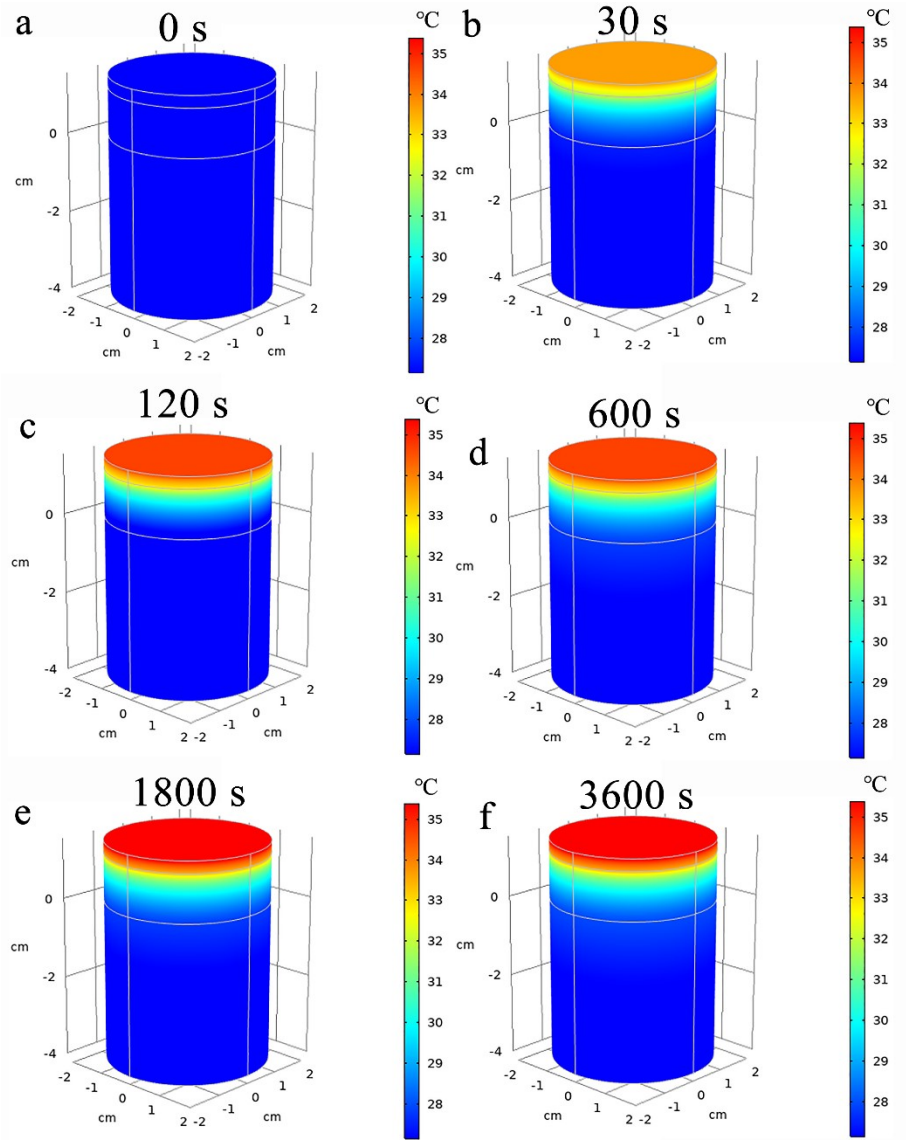

Figure S8. Transient state simulation of temperature distributions of WBE model at (a) 0 s, (b) 30 s, (c) 120 s, (d) 600 s, (e) 1800 s, (f) 3600 s, respectively.

9. Photograph of the evaporation device.

Figure S9. The optical images of indoor evaporation measurement.

10. Raman spectra characterization.

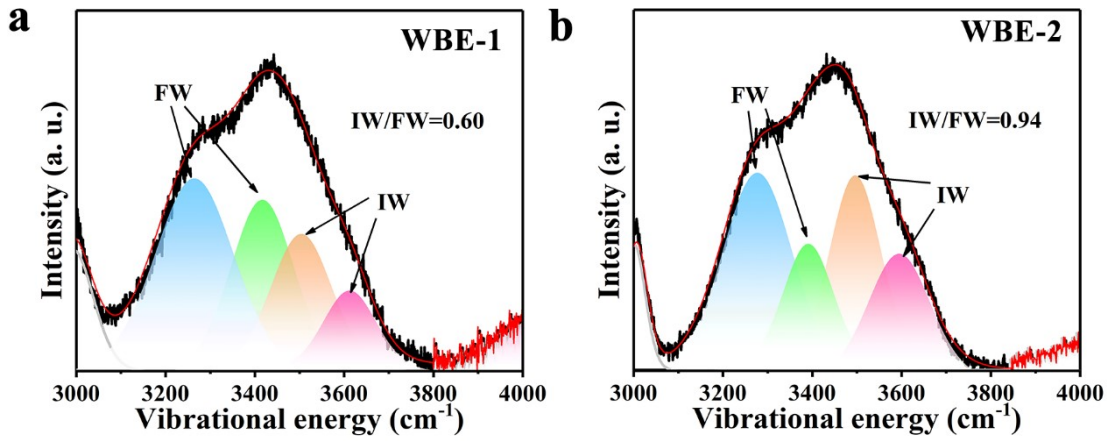

Figure S10. Fitting curves in energy region of O-H stretching modes for a) WBE-1 and b) WBE-2.

11. DSC spectra characterization.

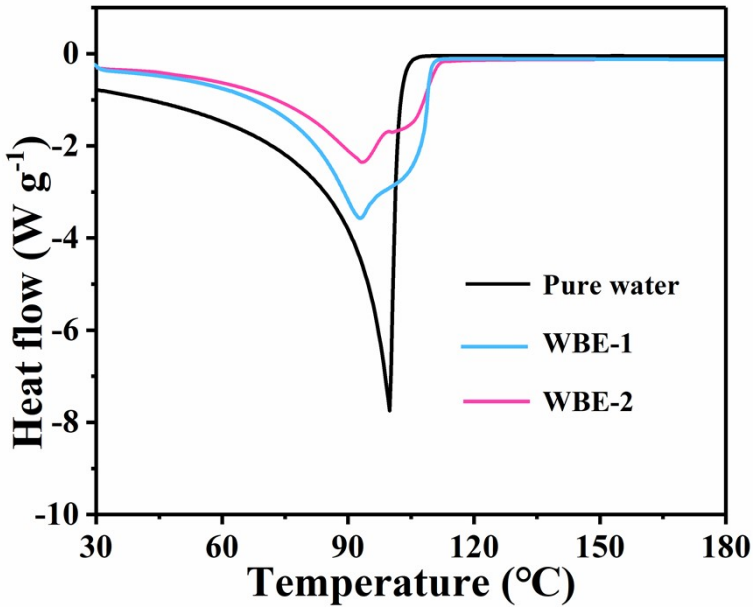

Figure S11. DSC curves of pure water, WBE-1, and WBE-2.

12. Brine addition process.

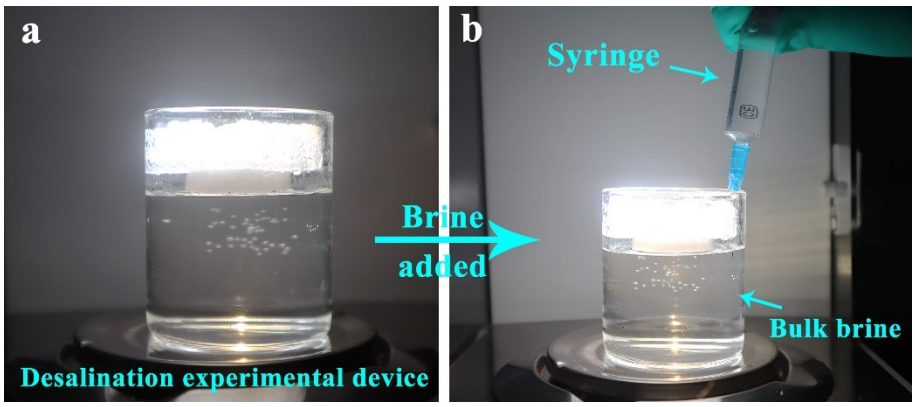

Figure S12. The brine addition process of desalination experiment.

13. Structural stability measurement.

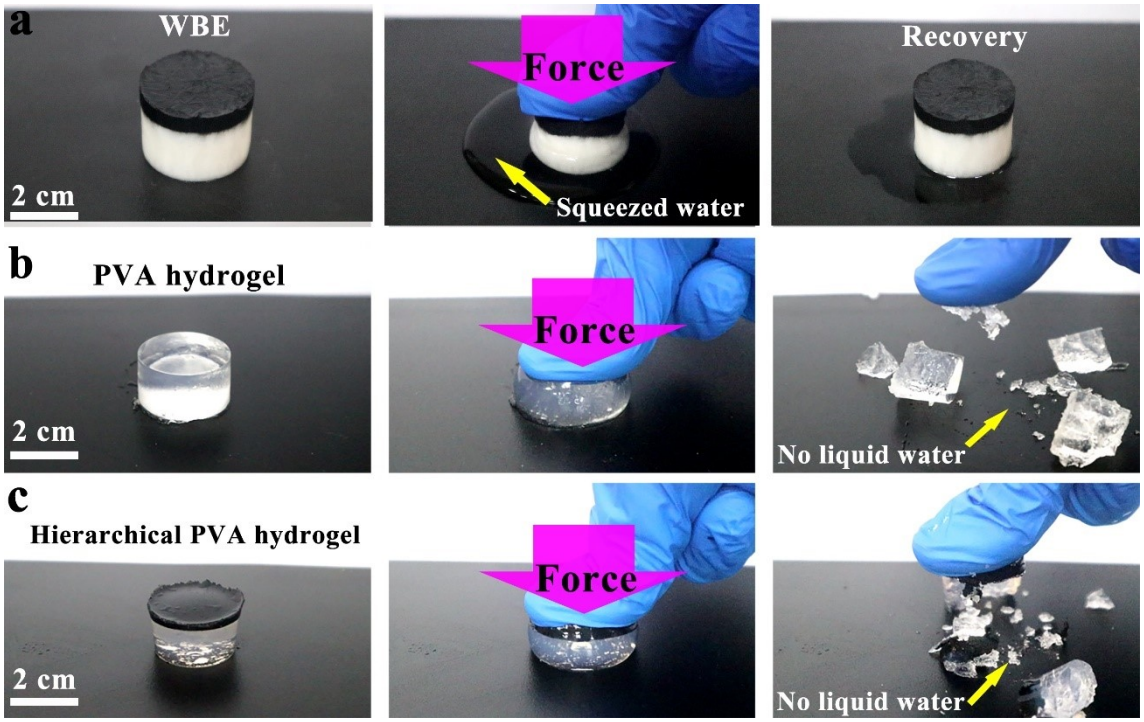

Figure S13. Photographs of deformation induced water release showing the pressed and recovered states of (a) WBE, (b) PVA hydrogel, and (c) hierarchical PVA hydrogel without CNFs addition.

14. Compressive stress-strain curve.

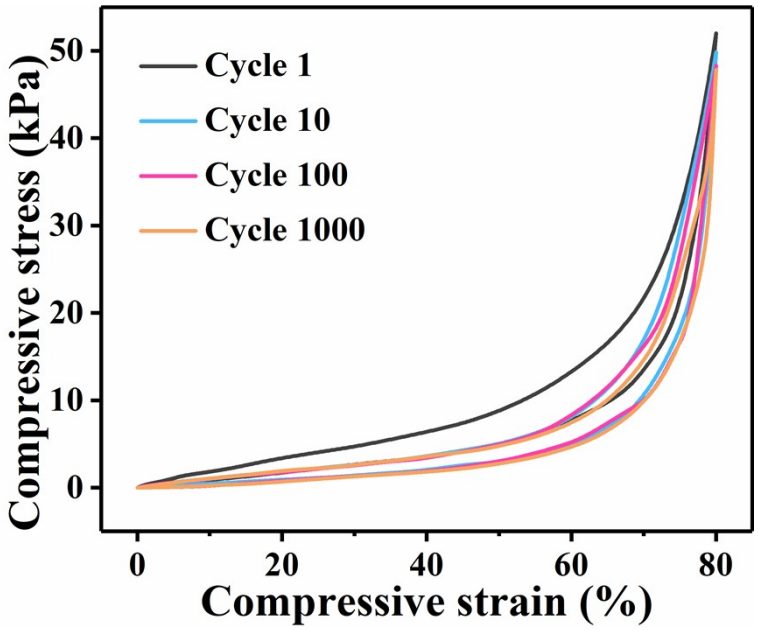

Figure S14. The compression σ–ε curves of the WBE at various maximum setting ε under brine.

15. Evaporation performance of WBE at different solutions.

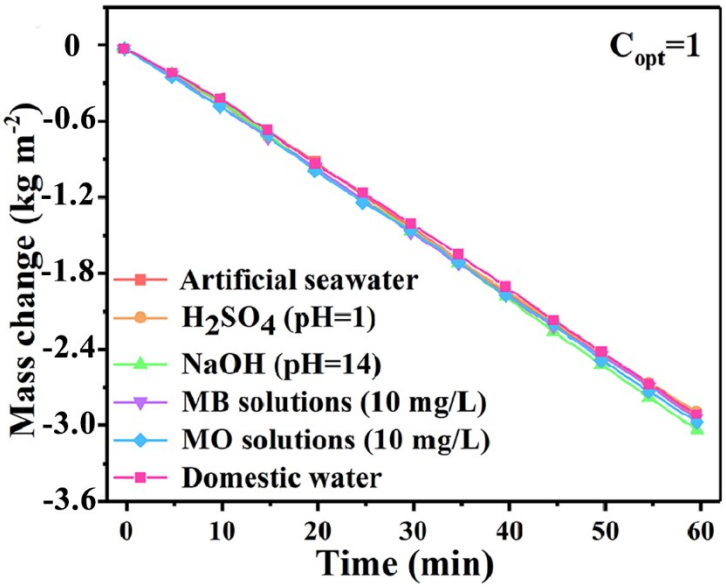

Figure S15. Mass changes of WBE in different solutions under 1 sun illumination.

16. PH value measurement of solution before and after evaporation.

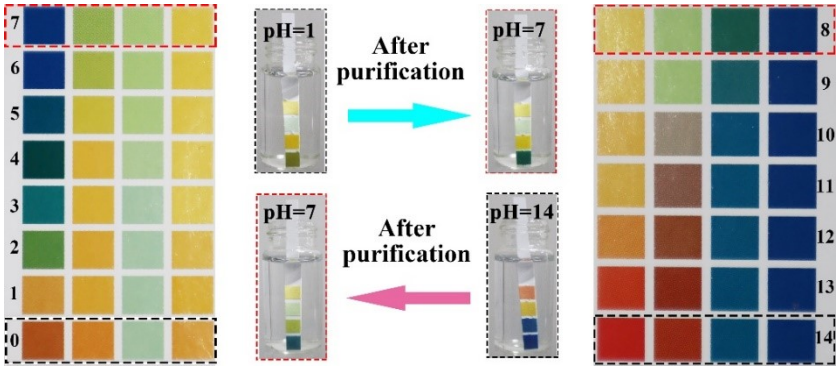

Figure S16. Comparison of the pH value of acidic water and alkaline water before and after evaporation.

17. Water quality measurement of domestic water.

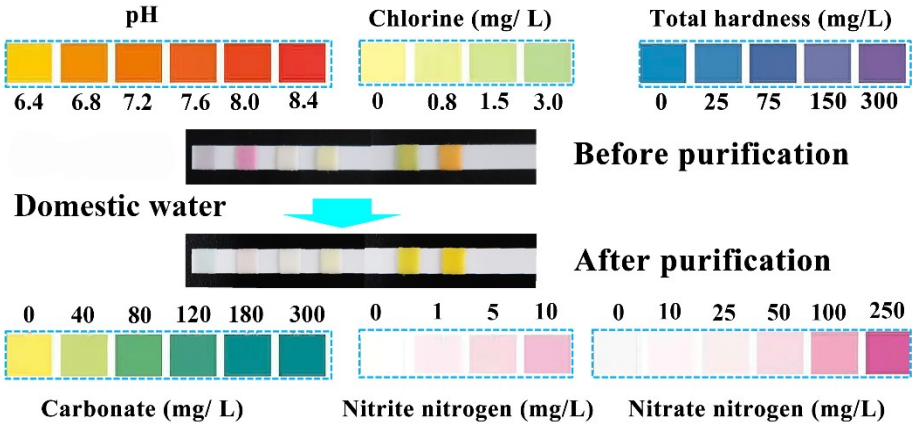

Figure S17. Domestic water quality tests of Xi'an, Shaanxi before and after solar evaporation using WBE.

18. Photograph of outdoor evaporation device.

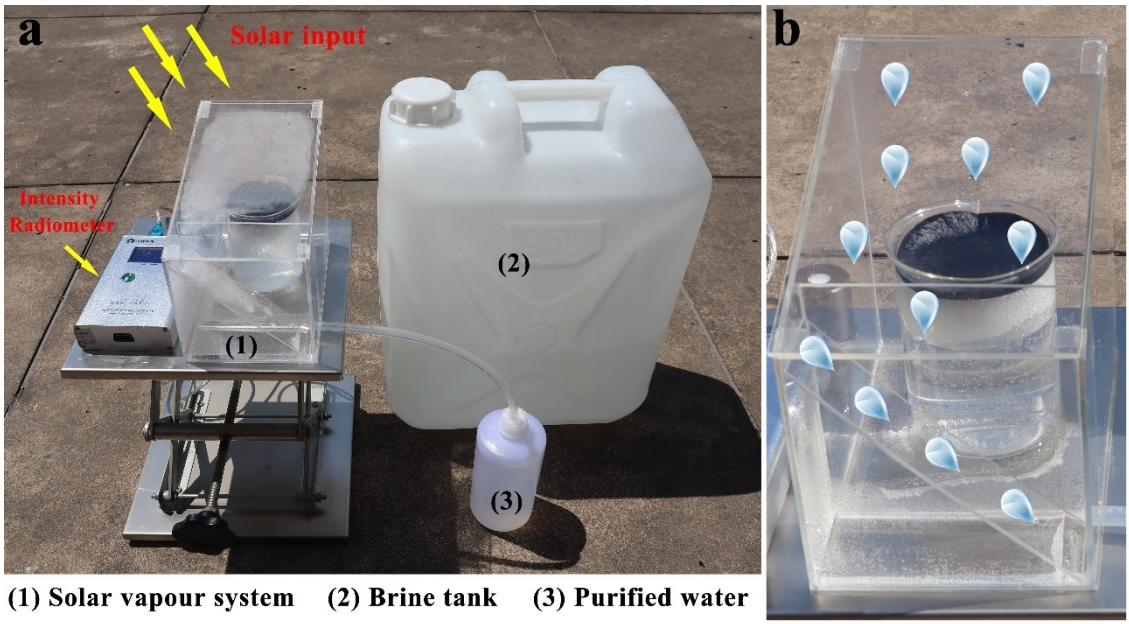

(1) Solar vapour system (2) Brine tank (3) Purified water

Figure S18. (a) A self-made solar evaporation water collection device was deployed on the roof. (b) Water collection process. Outdoor evaporation measurements were carried out on a sunny day (9:00-17:00) in Xi'an, China. A self-made solar evaporation water collection device was deployed on the roof of a 20 m high building. The sides of the solar steam generation and collection unit are customized to a trapezoidal structure with the top water collection plate at an angle of approximately 30° to the horizontal so that condensed water vapor can slide off. The collected water can be pooled by connecting the collection device and the plastic bottle through a conduit.

References

1. H. Wang, R. Zhang, D. Yuan, S. Xu, L. Wang, *Adv. Funct. Mater.*, 2020, **30**, 2003995.
2. X. Liu, F. Chen, Y. Li, H. Jiang, D. D. Mishra, F. Yu, Z. Chen, C. Hu, Y. Chen, L. Qu, W. Zheng, *Adv. Mater.*, 2022, **34**, 2203137.
3. F. Zhao, X. Zhou, Y. Shi, X. Qian, M. Alexander, X. Zhao, S. Mendez, R. Yang, L. Qu, G. Yu, *Nat. Nanotechnol.*, 2018, **13**, 489.
4. Z. Wang, Y. Yan, X. Shen, C. Jin, Q. Sun, H. Li, *J. Mater. Chem. A*, 2019, **7**, 20706-20712.
5. H. Sun, Y. Li, J. Li, Z. Zhu, W. Zhang, W. Liang, C. Ma, A. Li, *ACS Appl. Mater. Inter*, 2021, **13**, 33427–33436.
6. S. Tian, Z. Huang, J. Tan, X. Cui, Y. Xiao, Y. Wan, X. Li, Q. Zhao, S. Li, C.-S. Lee, *ACS Energy Lett.*, 2020, **5**, 2698–2705.
7. J. Xiao, Y. Guo, W. Luo, D. Wang, S. Zhong, Y. Yue, C. Han, R. Lv, J. Feng, J. Wang, W. Huang, X. Tian, W. Xiao, Y. Shen, *Nano Energy*., 2021, **87**, 106213.
8. N. Li, L. Qiao, J. He, S. Wang, L. Yu, P. Murto, X. Li, X. Xu, *Adv. Funct. Mater.*, 2020, **31**, 2008681.
9. C. Tian, C. Li, D. Chen, Y. Li, L. Xing, X. Tian, Y. Cao, W. Huang, Z. Liu, Y. Shen, *J. Mater. Chem. A.* 2021, **9**, 15462 -15471.
10. J. Lee, K. Kim, S. H. Park, G. Y. Yoon. J. Kim, S. J. Lee, *Nano Energy*, 2020, **77**, 105130.
11. Z. Huang, Y. Wan, J. Liang, Y. Xiao, X. Li, X. Cui, S. Tian, Q. Zhao, S. Li, C.-S. Lee, *ACS Appl. Mater. Inter.*, 2021, **13**, 31624–31634.

12. F. Li, N. Li, S. Wang, L. Qiao, L. Yu, P. Murto, X. Xu, *Adv. Funct. Mater.*, 2021, **31**, 2104464.

13. X. Han, S. Ding, L. Fan, Y. Zhou, S. Wang, *J. Mater. Chem. A*, 2021, **9**, 18614 - 18622.

14. T. Xu, Y. Xu, J. Wang, H. Lu, W. Liu, J. Wang, *Chem. Eng. J.*, 2021, **415**, 128893.

15. H. Liu, R. Jin, S. Duan, Y. Ju, Z. Wang, K. Yang, B. Wang, B. Wang, Y. Yao, F. Chen, *Small*, 2021, **32**, 2100969.

16. L. Wu, Z. Dong, Z. Cai, T. Ganapathy, N. X. Fang, C. Li, C. Yu, Y. Zhang, Y. Song, *Nat. Commun.*, 2020, **11**, 521.

17. Y. Chen, J. Yang, L. Zhu, X. Jia, S. Wang, Y. Li, H. Song, *J. Mater. Chem. A*, 2021, **9**, 15482-15492.

18. R. Zhu, D. Wang, J. Xie, Y. Liu, M. Liu, S. Fu, *Chem. Eng. J.*, 2022, **427**, 131618.

19. M. Zou, Y. Zhang, Z. Cai, C. Li, Z. Sun, C. Yu, Z. Dong, L. Wu, Y. Song, *Adv. Mater.*, 2021, **33**, 2102443.

20. W. Zhao, H. Gong, Y. Song, B. Li, N. Xu, X. Min, G. Liu, B. Zhu, L. Zhou, X.-X. Zhang, J. Zhu, *Adv. Funct. Mater.*, 2021, **31**, 2100025.

21. Y. Kuang, C. Chen, S. He, E. M. Hitz, Y. Wang, W. Gan, R. Mi, L. Hu, *Adv. Mater.*, 2019, **31**, 1900498.

22. X. Wu, Y. Wang, P. Wu, J. Zhao, Y. Lu, X. Yang, H. Xu, *Adv. Funct. Mater.*, 2021, **31**, 2102618.